# Dynamic soil stiffness for foundation piles

## Capturing 3D continuum effects in an effective, non-local 1D model

Versteijlen, W. G.; de Oliveira Barbosa, J. M.; van Dalen, K. N.; Metrikine, A. V.

**DOI**
10.1016/j.ijsolstr.2017.11.007

**Publication date**
2018

**Document Version**
Accepted author manuscript

**Published in**
International Journal of Solids and Structures

# Dynamic soil stiffness for foundation piles: capturing 3D continuum effects in an effective, non-local 1D model

W G Versteijlen[a,b], J M de Oliveira Barbosa[b], K N van Dalen[b], A V Metrikine[b]

[a]*Siemens Wind Power, Beatrixlaan 800, 2595 BN Den Haag, The Netherlands*
[b]*Faculty of Civil Engineering and Geosciences, Delft University of Technology, Stevinweg 1, 2628CN Delft, The Netherlands*

**Abstract**

A method is presented to accurately capture the 3D interaction phenomena of a foundation pile embedded in soil, in a computationally efficient non-local 1D model. It is shown how to extract the global stiffness kernels from simulations with the 3D inhomogeneous continuum, and implement them in a 1D non-local Winkler-type model that can subsequently serve as a stand-alone, condensed substructure. The presented method for obtaining the kernels removes the need to assume certain distributions for these functions. We show that the method is very versatile, and yields accurate results for a wide range of pile geometries and soil stiffness profiles, over the full depth of the embedded pile. For the dynamic case, the discretized global stiffness kernels (matrices) become complex-valued (they include soil stiffness, inertia and damping), and the 1D model proves to be capable of mimicking also the out-of-phase part of the response. The method being straightforward and fast, the engineering community is served the benefits of accuracy (3D model) and speed (1D model), without the need of empiric tuning.

*Keywords:* non-local dynamic stiffness, 3D soil-structure effects, effective 1D soil stiffness, effective 1D soil damping, offshore wind foundations, substructuring

# 1. Introduction

The methods capturing the complex soil-structure interaction (SSI) have varied over the last 2 centuries, depending on the application and computational power. On the one hand, closed form analytical solutions exist for the case of homogeneous soil and a relatively simple, symmetric structure [1] - [4]. These are fast and can be quite accurate. A completely different approach has been enabled by the modern capabilities of capturing the interaction using computationally intensive numerical/semi-numerical methods that can model complex-shaped structures and inhomogeneous soil [5]. Computational power is ever-increasing, however, the demand in terms of precision and complexity of these numerical methods increases accordingly, making them time-expensive and therefore only fit for 'once-of' simulations. The broad spectrum of methods in between these two (analytical versus numerical) could be characterized by a mixture of both methods, including empirical tuning. The high variability of in-situ soil properties (for instance strain, stress or load-history dependence, some of which are still not fully understood to date [6, 7]) calls for efficient methods that are developed on the basis of test verifications and tuning of a theoretical framework. Such semi-emperical methods have allowed for safe construction of challenging civil engineering structures without having to use expensive simulation algo-

rithms. For example, the tuning coefficients of Terzaghi [8] made the theory of *subgrade reaction* [1, 9] practically useable in the railroad industry, and for piled foundations. Nevertheless, the theoretical frameworks with associated parameter tuning are bound to their original application, and should be cautiously applied to SSI cases of which either the structure or the soil no longer coincides with the original framework. An example of this is encountered in the offshore wind industry, the origin of motivation for the current work. In this industry the *p-y* curve method, which was once developed for modelling large lateral displacements of long flexible piles [10] - [12], is still used for modelling the small-strain soil reaction against the short, rigidly behaving piles used in offshore wind today [13, 14].

Along with the development of rigorous numerical models, comes the need to translate those into simpler models, combining the best of both: accuracy and computational speed [15]. The latter is a requisite for some application fields, where numerous load cases need to be simulated. Besides speed, simple models may facilitate improved understanding of the fundamental physics behind the problem at hand. In our application field of offshore wind turbine foundations, the design of large-diameter, thin-walled, rigidly behaving piles call for 3D SSI

simulations. A 3D model automatically captures the complex interaction phenomena for these piles, which, besides the lateral soil stiffness (being the main reaction principle for flexible piles), also includes significant rotational stiffness components and pile-tip shearing effects [16]. To employ the accuracy of a 3D model for engineering purposes (expensive time-domain simulations), we have previously proposed a translation method to find an effective 1D stiffness (subgrade reaction) that represents the 3D soil reaction in the case of multi-layered soils [17]. The method introduced in [17] provides a substructure in the form of a Winkler foundation stiffness in which the lateral springs are uncoupled (i.e., *local* spring stiffness).

In the current work a method is introduced to extract and use a *non-local* Winkler-type stiffness that couples the reaction forces of the soil in interaction with the pile over the full embedment length. As will be explained in Section 3.1, capturing the global soil reaction mechanisms is a requisite for accurately modelling rigidly behaving foundations. It is demonstrated that the proposed method has great potential as the discretized stiffness kernels of the 3D model (Section 2.2) can be applied in a wide range of soil-pile systems (Sections 3.1 & 3.2), without the need of any further discrete correction springs. Moreover, the presented non-local method holds the advantage that the stiffness kernels

are obtained in a single, direct action, whereas the previously published local stiffness method [17] involves an optimization process to find an appropriate effective 1D stiffness. Similar to that method, determining the 3D reaction (captured in the stiffness kernels in this case) has to be performed only once, after which the obtained 1D effective model is to be used as a stand-alone, condensed model for extensive design simulations. For the linear elastic case, 3D simulations can still be relatively fast. However, the gain in computational efficiency due to the significant reduction of the number of degrees of freedom in the transition from a 3D model towards a 1D model, becomes substantial for application fields where thousands of simulations are required. For example, due to the stochastic nature of the loading environment of offshore wind turbines, currently about 120,000 10-min time-domain (for capturing the non-linear aeroelastic interaction) simulations are performed for an average design case. Significantly decreasing the number of degrees of freedom of the design model with negligible loss of accuracy, is clearly a large gain in such a design community.

Other researchers have studied the capabilities of non-local elasticity as well. However, where they assume certain distributions for the associated kernel func-

tions [18, 19], the here proposed method shows how to directly obtain these functions from the 3D model - the specific novelty of the current paper. The choice of condensing towards a full Winkler-type model instead of for instance a lumped parameter model, stems from the strong desire of the engineering community to employ such 1D models. Winkler-type models have the advantage of increased physical insight as they directly yield the distribution of stresses within, and displacements of the pile. Therefore, other than only considering the pilehead displacements (as is often done [16, 20]), we consider the match in response of the entire embedded pile in terms of its displacement, slope, rotation and curvature. A great benefit of the method is that, for a dynamic simulation, the 3D complex stiffness (i.e. including soil damping) can be directly integrated in the 1D effective model, so that the out-of-phase part of the 3D response will also be matched (Section 3.3). Therefore, simply an estimate of the intrinsic material damping properties related to the type of soil can be used in defining the complex-valued Young's modulus of the 3D model, and an accurate 1D effective model can be directly derived that captures the material and geometric damping of the 3D model. In Section 4 we discuss the remaining small discrepancies between the 3D and 1D response, and how these could be minimized even further.

## 2. Method

The non-local stiffness method comprises two steps: first, the global stiffness kernels need to be extracted from the 3D continuum (Section 2.2), and second, these stiffness kernels need to be integrated in the 1D beam model (Section 2.3). The non-local stiffness method can be used for any type of solution; it may be a semi-analytical solution approach, or a numerical one using, for instance, finite elements. In this paper, the continuum is modelled with finite elements, and the governing equations of the 1D integrated beam model (discussed in the next section) are solved using the finite difference (FD) method.

### 2.1. Governing equations of the 1D model

We use the Timoshenko beam on a distributed, Winkler-type foundation model as the basis for the 1D effective model. The equilibrium equations for the local, static model are

$$GA\kappa\Big(\frac{d^2u(z)}{dz^2} - \frac{d\psi(z)}{dz}\Big) - f(z,u,\psi) = 0, \tag{1}$$

$$GA\kappa\Big(\frac{du(z)}{dz} - \psi(z)\Big) + EI\frac{d^2\psi(z)}{dz^2} - m(z,u,\psi) = 0, \tag{2}$$

where Eq. 1 describes the balance of lateral forces, and Eq. 2 describes the balance of bending moments. In these equations, $u(z)$ and $\psi(z)$ are the displacement and rotation of the pile, respectively. $f(z,u,\psi)$ and $m(z,u,\psi)$ are

respectively the distributed restoring force and moment of the soil. $EI$ is the product of the Young's modulus of the structural steel $E$ and the second moment of area of the cross section of the pile $I$. Furthermore, $GA\kappa$ is the product of the shear modulus of the structural steel $G$, the area of the cross section $A$ and $\kappa$, the cross section-dependent Timoshenko shearing coefficient. For the shape of the cylindrical cross section of the pile, $\kappa = 0.53$ is assumed. The sign convention of the 1D model is given in Figure 1, in which the conventional case is shown where $f(z, u, \psi)$ reduces to $f(z, u)$ and equals $k(z)u$, and $m(z, u, \psi) = 0$. Here $k(z)$ is the local Winkler stiffness (often called the modulus of horizontal subgrade reaction [8, 11]). The following boundary conditions apply:

$$GA\kappa(\tfrac{du}{dz} - \psi)\Big|_{z=0} = -F, \tag{3}$$

$$EI\tfrac{d\psi}{dz}\Big|_{z=0} = M, \tag{4}$$

$$GA\kappa(\tfrac{du}{dz} - \psi)\Big|_{z=L} = 0, \tag{5}$$

$$EI\tfrac{d\psi}{dz}\Big|_{z=L} = 0, \tag{6}$$

signifying that (from top to bottom) a lateral excitation force $F$ and overturning moment $M$ are applied to the top of the pile, and that the tip of the pile is free (zero shear force and moment).

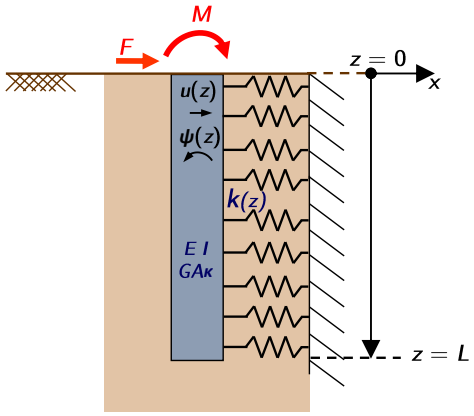


Figure 1: Graphical representation of the local 1D beam model and the used sign convention.

Introducing the non-local stiffness operator, the restoring force term $f(z, u, \psi)$ in the force equilibrium, Eq. 1, becomes an integral:

$$GA\kappa\Big(\frac{d^2u(z)}{dz^2} - \frac{d\psi(z)}{dz}\Big) - \int_0^L K^{\mathrm{u,u}}(z,\overline{z})u(\overline{z})d\overline{z} = 0, \tag{7}$$

signifying that the lateral restoring force of the soil on the pile at a location $z$ is the product of the displacement of the pile $u(z)$ and stiffness of the soil $K^{\mathrm{u,u}}(z, \overline{z} = z)$ at that particular location (similar as in the local approach), *and* of the pile displacements $u(\overline{z})$ and stiffness of the soil $K^{\mathrm{u,u}}(z, \overline{z})$ at all other locations along the pile; the latter are the non-local contributions. Note that although the integral in Eq. 7 only covers the domain of the pile (from 0 to $L$), the forces exerted on the pile are the reaction of the continuum as a whole (which extends beyond $z = L$). This is implicit in the stiffness kernel; $K^{\mathrm{u,u}}(z, \overline{z})$ is derived based on the 3D reaction of the entire medium (as will be described

in Section 2.2).

Incorporating also other continuum-related effects like the rotational stiffness $K^{\Psi,\Psi}$ and the stiffness operators for coupling the lateral stiffness with rotations $K^{\mathrm{u},\Psi}$ and vice versa $K^{\Psi,\mathrm{u}}$, we get

$$GA\kappa\Big(\frac{d^2u(z)}{dz^2} - \frac{d\psi(z)}{dz}\Big) - \int_0^L K^{\mathrm{u},\mathrm{u}}(z,\overline{z})u(\overline{z})d\overline{z} - \int_0^L K^{\mathrm{u},\Psi}(z,\overline{z})\psi(\overline{z})d\overline{z} \quad = 0, \quad (8)$$

$$GA\kappa\Big(\frac{du(z)}{dz} - \psi(z)\Big) + EI\frac{d^2\psi(z)}{dz^2} - \int_0^L K^{\Psi,\Psi}(z,\overline{z})\psi(\overline{z})d\overline{z} - \int_0^L K^{\Psi,\mathrm{u}}(z,\overline{z})u(\overline{z})d\overline{z} \quad = 0 \quad (9)$$

The next section explains how to retrieve the global stiffness kernels $K(z,\overline{z})$ from a 3D FE continuum model, and Section 2.3 elaborates on implementing these terms in a FD scheme for solving the 1D governing equations (Eqs. 8 and 9).

## 2.2. Extracting the 3D continuum reaction

For modelling the reaction of the 3D stratified soil continuum, a FE model was built using solid elements. To extract the global stiffness kernels, the soil should be modelled including a cavity for the pile; no stiffness of the steel should be incorporated as these stiffness kernels should only represent the soil reaction. The stiffness of the pile in the 1D model is represented by the first term in Eq. 8 and the first two terms in Eq. 9. We refer to the space occupied by the pile as

the 'cavity' in the 3D model; this is the space the steel of the pile would occupy if it were modelled. Furthermore, if the volume within the pile is to be modelled as only partly filled with soil, such a void needs to be created at this location in the 3D continuum. In this paper we will consider piles that are fully filled with soil. Figure 2 shows the FE mesh of (part of) the soil domain, with a cavity for a pile that is fully filled with soil, with a vertical discretization $h = 0.5$ m and a 1 m soil layer thickness. When using a numerical solution method, the global stiffness kernels ($K^{\mathrm{u,u}}(z,\overline{z})$,..,$K^{\Psi,\mathrm{u}}(z,\overline{z})$) will be discretized into stiffness matrices of size $n \times n$, with $n$ the amount of nodes employed to discretize the vertical axis of the 1D model. The terms of the stiffness matrices will depend on the properties of the soil and the diameter $D$ of the pile. In this paper, for ease of explanation, the 3D pile and adjacent soil (and consequently also the 1D model) have a regular mesh with fixed vertical discretization size $h$. However, it is noted that the presented method can be generalized to any mesh shape.

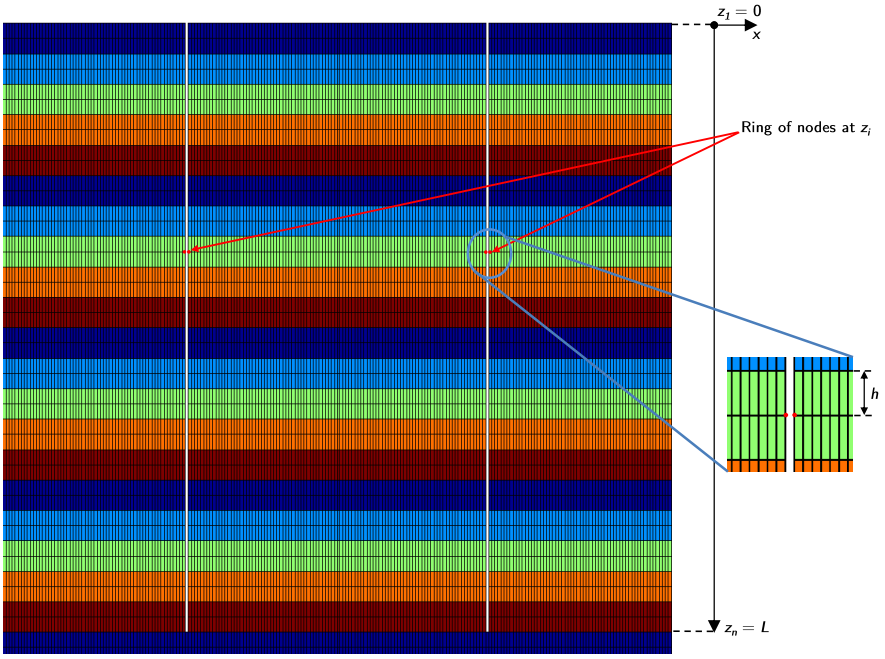


Figure 2: Example of the FE mesh, showing the cavity of a pile (with a diameter of 10 m and thickness of 0.1 m) that is fully filled with soil, with a vertical discretization $h = 0.5$ m and 1 m soil layer thickness. Only part of the soil domain is shown.

The extraction of the lateral stiffness matrix $\mathbf{K}^{\mathrm{u,u}}$ is straightforward. With reference to Figure 2, for every discrete depth $z_i$ (with $i = 1, .., n$, and discretization length $h$, the mudline at $z_1 = 0$ and pile tip at $z_n = L$), we displace the circumferential ring of nodes of the cavity surface with a certain displacement $u_i$ in $x$-direction (see Figure 1) and collect the sum of the nodal horizontal reaction forces at that ring, but also at all other vertically spaced rings, at depths $z_{j \neq i}$. We thus fill a matrix $\mathbf{F}_{\mathrm{x}}$ with column vectors $f_{x,j}$ being the reaction forces at depths $z_j$ due to the displacements in the continuum at depths $z_i$. The pre-

scribed displacements are collected in $\mathbf{U}$, which is a diagonal matrix. To be consistent with the integral of Eq. 8, we furthermore introduce an auxiliary matrix $\tilde{\mathbf{U}}$ which incorporates the Trapezium rule for integration:

$$\tilde{U}_{i,j} = \begin{cases} \frac{1}{2} h U_{i,j}, & \text{for } i = 1 \text{ and } i = n, \\ h U_{i,j}, & \text{otherwise.} \end{cases} \tag{10}$$

With these matrices known, we can readily compute the stiffness matrix $\mathbf{K}^{\mathrm{u,u}}$. To derive the stiffness matrix that can be used in the integral of Eq. 8, we write

$$\frac{1}{h} \begin{bmatrix} . & \uparrow & . \\ . & [f_{x,j}] & . \\ . & \downarrow & . \end{bmatrix} = \begin{bmatrix} & \mathbf{K}^{\mathrm{u,u}} & \end{bmatrix} \begin{bmatrix} \tilde{U}_{1,1} & 0 & 0 \\ 0 & \tilde{U}_{i,i} & 0 \\ 0 & 0 & \tilde{U}_{n,n} \end{bmatrix}. \tag{11}$$

Note that the unit of the lateral equilibrium forces (Eq. 7) is N/m, therefore, in Eq. 11, the nodal force matrix $\mathbf{F}_{\mathrm{x}}$ is divided by the discretization length $h$. Now we can readily find the stiffness matrix as

$$\mathbf{K}^{\mathrm{u,u}} = \frac{\mathbf{F}_{\mathrm{x}} \tilde{\mathbf{U}}^{-1}}{h}. \tag{12}$$

In a similar way, the rotational stiffness matrix $\mathbf{K}^{\Psi,\Psi}$ can be found by imposing a rotation $\psi_i$ on the nodal rings along the circumference of the cavity surface, collecting the nodal reaction forces in vertical direction for all depths $f_{z,j}$, and thus form the matrix $\mathbf{F}_{\mathrm{z}}$. The rotational stiffness relates the rotations to the

distributed moment, so we incorporate the lever arm $D/2$ at which the vertical soil reaction forces act with respect to the central axis of the pile:

$$\mathbf{K}^{\psi,\psi} = \frac{D\mathbf{F}_{\mathrm{z}}\tilde{\mathbf{\Psi}}^{-1}}{2h}, \tag{13}$$

in which $\tilde{\mathbf{\Psi}}$ is the matrix containing the imposed rotations, adjusted to incorporate the trapezium rule in a similar way as is done for the displacements (Eq. 10). Then, the coupling stiffness matrix for the lateral reaction to rotations of the nodal rings is found as

$$\mathbf{K}^{\mathrm{u},\psi} = \frac{\mathbf{F}_{\mathrm{x}}\tilde{\mathbf{\Psi}}^{-1}}{h}, \tag{14}$$

and the coupling stiffness matrix for the rotational reaction to lateral displacements of the nodal rings as

$$\mathbf{K}^{\psi,\mathrm{u}} = \frac{D\mathbf{F}_{\mathrm{z}}\tilde{\mathbf{U}}^{-1}}{2h}. \tag{15}$$

Figure 3 shows examples of the four stiffness matrices (Eqs. 12 - 15) for a cavity of 5 m diameter, thickness of 0.06 m, 25 m embedment length, modelled with an element length of $h = 0.25$ m, embedded in a stratified soil that will be discussed in Section 3.1. $\mathbf{K}^{\psi,\psi}$ and $\mathbf{K}^{\mathrm{u},\mathrm{u}}$ are symmetric matrices, whereas $\mathbf{K}^{\psi,\mathrm{u}}$ and $\mathbf{K}^{\mathrm{u},\psi}$ have the following interrelation:

$$K^{\psi,\mathrm{u}}_{i,j} = K^{\mathrm{u},\psi}_{j,i}. \tag{16}$$

It can be shown that this particular dependence is a direct consequence of the Maxwell-Betti reciprocal work theorem (e.g. [21]), or, for the dynamic case presented in Section 3.3, the elastodynamic source-receiver reciprocity relation (e.g. [22]).

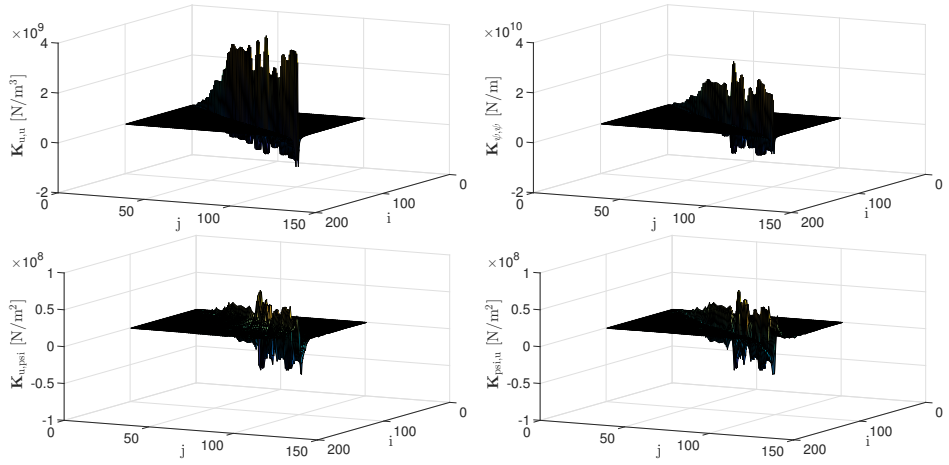


Figure 3: Example of $\mathbf{K}_{\mathrm{u,u}}$, $\mathbf{K}_{\psi,\psi}$, $\mathbf{K}_{\psi,\mathrm{u}}$ and $\mathbf{K}_{\mathrm{u},\psi}$, shown in a clockwise order. The cavity has a length of 25 m, a diameter of 5 m and was discretized with $h$=0.25 m. The soil profile is "CPT20", given in Section 3.1.

The next section covers the implementation of the global stiffness matrices in a FD scheme to solve the 1D beam equations.

## 2.3. Implementation in a 1D model

We use Euler's central finite difference schemes [23] to approximate the solution of a Timoshenko beam on a non-local Winkler foundation. Let $u$ and $\psi$ be sufficiently smooth functions of $z$, which we wish to evaluate in a domain of length $L$ at $n$ equally spaced points, creating a discretization length $h = L/(n-1)$. In this schematization, we approximate (with error $O(h^2)$) the first and

second derivative terms of Eqs. 8 and 9, and write - invoking summation over repeated indices:

$$\frac{GA\kappa}{h^2}(u_{i-1} - 2u_i + u_{i+1}) - \tilde{K}^{\mathrm{u,u}}_{i,j} u_j - \frac{GA\kappa}{2h}(-\psi_{i-1} + \psi_{i+1}) - \tilde{K}^{\mathrm{u},\Psi}_{i,j}\psi_j = 0, \tag{17}$$

$$\frac{GA\kappa}{2h}(-u_{i-1} + u_{i+1}) - \tilde{K}^{\Psi,\mathrm{u}}_{i,j} u_j - GA\kappa\psi_i + \frac{EI}{h^2}(\psi_{i-1} - 2\psi_i + \psi_{i+1}) - \tilde{K}^{\Psi,\Psi}_{i,j}\psi_j = 0, \tag{18}$$

with $i = 1, .., n$ and $j = 0, .., n+1$, $z_1 = 0$ representing the location of the pile head and $z_n = L$ that of the pile tip. This implies we use 2 ghost nodes ($j = 0$ and $j = n+1$) to solve the equations at the boundaries of the domain. Similar to Eq. 10, the tilde over the global stiffness matrices ($\tilde{K}^{\mathrm{u,u}}_{i,j}$, .. ,$\tilde{K}^{\Psi,\mathrm{u}}_{i,j}$) in Eqs. 17 and 18 indicates that these matrices are auxiliary matrices, incorporating the Trapezium rule modifications, where in this case the first and last columns of the original stiffness matrices are multiplied by $\frac{1}{2}$:

$$\tilde{K}^{\mathrm{u,u}}_{i,j} = \begin{cases} \frac{1}{2}hK^{\mathrm{u,u}}_{i,j}, & \text{for } j = 1 \text{ and } j = n, \\ hK^{\mathrm{u,u}}_{i,j}, & \text{otherwise,} \end{cases} \tag{19}$$

with $K^{\mathrm{u,u}}_{i,j}$ the stiffness matrix calculated in Eq. 12. Furthermore, a column of zeros is added to the left and right side of the matrix to incorporate the ghost nodes:

$$\tilde{K}^{\mathrm{u,u}}_{i,j} = 0, \text{ for } j = 0 \text{ and } j = n+1. \tag{20}$$

$\tilde{K}^{\mathrm{u},\Psi}_{i,j}$, $\tilde{K}^{\Psi,\mathrm{u}}_{i,j}$ and $\tilde{K}^{\Psi,\Psi}_{i,j}$ incorporate similar modifications.

Next we rewrite the boundary conditions (Eqs. 3 - 6), isolating the ghost nodes:

$$GA\kappa(\frac{-u_0+u_2}{2h} - \psi_1) = -F,$$
$$u_0 = \frac{2h}{GA\kappa}F - 2h\psi_1 + u_2, \tag{21}$$

$$EI(\frac{-\psi_0+\psi_2}{2h}) = M,$$
$$\psi_0 = \frac{-2h}{EI}M + \psi_2, \tag{22}$$

$$GA\kappa(\frac{-u_{n-1}+u_{n+1}}{2h} - \psi_n) = 0,$$
$$u_{n+1} = 2h\psi_n + u_{n-1}, \tag{23}$$

230

$$EI(\frac{-\psi_{n-1}+\psi_{n+1}}{2h}) = 0,$$
$$\psi_{n+1} = \psi_{n-1}. \tag{24}$$

These expressions need to be substituted into the system of equations given by 17 and 18 for $i = 1$ and $i = n$ in order to eliminate the ghost nodes. Doing so for the first equilibrium equation (17), for the upper boundary at $z_1$ (pile head), we obtain:

$$\frac{GA\kappa}{h^2}(-2u_1 + 2u_2) - \tilde{K}^{u,u}_{1,j}u_j - \frac{2GA\kappa}{h}\psi_1 - \tilde{K}^{u,\psi}_{1,j}\psi_j = -\frac{2F}{h} + \frac{GA\kappa M}{EI}, \tag{25}$$

and at the lower boundary $z_n$:

$$\frac{GA\kappa}{h^2}(2u_{n-1} - 2u_n) - \tilde{K}^{u,u}_{n,j}u_j + \frac{2GA\kappa}{h}\psi_n - \tilde{K}^{u,\psi}_{n,j}\psi_j = 0. \tag{26}$$

Similar for the second equilibrium equation 18, around the first point $i = 1$:

$$-\tilde{K}^{\psi,u}_{1,j}u_j + \frac{EI}{h^2}(-2\psi_1 + 2\psi_2) - \tilde{K}^{\psi,\psi}_{1,j}\psi_j = F + \frac{2M}{h}, \tag{27}$$

and the last equation, at the last point $i = n$:

$$-\tilde{K}^{\psi,u}_{n,j}u_j + \frac{EI}{h^2}(2\psi_{n-1} - 2\psi_n) - \tilde{K}^{\psi,\psi}_{n,j}\psi_j = 0. \tag{28}$$

For the inner domain, Eqs. 17 and 18 remain unchanged. The outer ghost nodes ($j = 0$ and $j = n + 1$) have now been eliminated, resulting in a square matrix that can be inverted; by collecting the terms in Eqs. 25 - 28 in a coefficient matrix $\mathbf{A}$ and a right hand side vector $\mathbf{b}$, we can find the solution vector $\mathbf{x}$ (containing $u$ and $\psi$) by solving the linear equation $\mathbf{Ax} = \mathbf{b}$.

# 3. Applications

In this section we demonstrate the potential of the technique. We will investigate how well the full 3D solution matches with the 1D non-local solution for different soil-pile combinations. From previous experience [17], it is known that the success rate of mimicking a 3D soil-pile response with a 1D effective model depends on the rigidity of the soil-pile system. Therefore, first a selection of 4 examples is presented in the next section. First we consider the static case (Section 3.2), and subsequently the dynamic case (Section 3.3), to see if the damping related to 3D reactions can also be captured by the approach.

## 3.1. Pile categorization & case selection

The degree of non-local interaction between the structure and the continuum depends on the flexibility of the system. The displacement profile of a flexible pile typically has multiple crossings of the zero-displacement line. While a

flexible pile evokes a more local reaction from the soil, a rigid pile makes the soil react in a global way; a larger part of the continuum is mobilized to counteract the rigid pile [24]. A local 1D Winkler foundation may suffice for flexible piles, but a 1D model for rigid pile behaviour needs additional features to capture the complex SSI. Often the ratio of the embedment length $L$ over the diameter $D$ is used to categorize piles in either slender, (long) flexible piles with a high $L/D$ ratio, or rigidly behaving piles that are short, with a low $L/D$ ratio. However, when only considering the pile geometry in this categorization, the interaction with the soil is neglected; a slender pile (high $L/D$) can still bend in a rigid way when embedded in very soft soil. A useful parameter that incorporates the soil stiffness in the soil-pile categorization is the pile flexibility factor introduced by Poulos and Hull [25], and used by Abadie [26]:

$$K_r = \frac{EI_p}{E_s L^4} \quad \begin{cases} > 0.208\text{: rigid pile behaviour,} \\ \\ < 0.0025\text{: flexible pile behaviour,} \end{cases} \tag{29}$$

in which $EI_p$ is the bending stiffness of the pile and $E_s$ the Young's modulus of the soil. The expression is based on the idea that for a homogeneous, linear elastic soil, there is a certain critical length ($L_c$) of the pile, beyond which a further increase of the length of the pile has no further influence on the pile head response [25]. The large precision in the boundaries of the behaviour type

seems a bit pretentious, however, together with the $L/D$ ratio, it enables us to graphically classify a few pile-soil systems, as is also done by Abadie [26]. Because the current research originates from the offshore wind industry, we here duplicate some of the typical values of installed monopile foundations and the piles originally used to calibrate the $p$-$y$ methodology, as shown in [26]. The latter paper, however, recommends to use the Young's modulus of the soil at pile-tip level as the value for $E_s$ in Eq. 29. Indeed, the pile-tip soil reaction is an important feature in the rigid pile behaviour, but we believe that the entire soil stratum should be taken into account. We therefore propose to take the mean value of the Young's modulus of the different soil layers. Secondly, Abadie uses rather low values of the Young's moduli of different soils: 50 MPa for dense sand, 3 MPa for soft to medium clay, and 30 MPa for stiff clay. Generally somewhat higher values are prescribed [27], and in our experience [17], [28], the small-strain Young's modulus for in-situ saturated dense sand can be in the order of 150 - 300 MPa. Because of these differences, we have multiplied the soil Young's modulus used for calculating the flexibility factors of the installed monopile foundations and $p$-$y$ development piles given by [26] by a factor of 5 (250 MPa/50 MPa). The resulting flexibility factors, together with the cases that will be evaluated in this paper are presented in Figure 4.

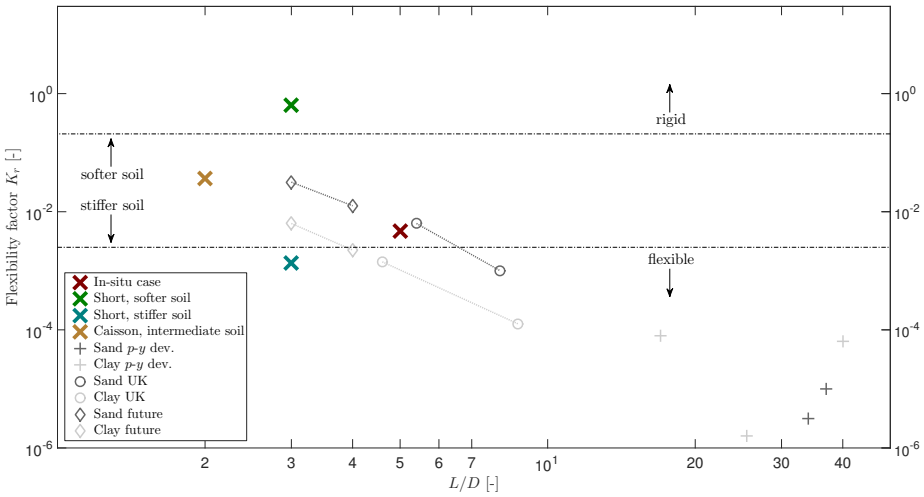


Figure 4: Flexibility factors and $L/D$ categorization. Note that the annotation for softer and stiffer soil applies for the same pile geometry; for 2 equal piles, an embedment in softer soil, yields more rigid behaviour.

As shown in Figure 4, 4 cases will be considered in this paper. The first case is called "In-situ" pile; this is a pile on which we conducted extensive measurements and for which we have previously performed a translation from a 3D to a 1D model, using a local technique (locally reacting springs) [28]. We further test the non-local technique for two short piles with a rather low $L/D = 3$, of which one pile is embedded in a relatively softer soil (the "Short-soft" case) and the other in a stiff soil (the "Short-stiff" case). Furthermore, we will consider a "Caisson" type pile: $L/D = 2$, embedded in stiff soil. The geometry of the cylindrical, thin-walled piles, the average Young's modulus $E_s$ and the flexibility factors of the 4 cases are given in Table 1.

| | $D$ | $L$ | $t$ | $E_s$ | $K_r$ |
|---|---|---|---|---|---|
| | [m] | [m] | [mm] | [MPa] | [-] |
| **In-situ** | 5 | 24 | 50 | 319 | 0.0047 |
| **Short-soft** | 10 | 30 | 100 | 15 | 0.6437 |
| **Short-stiff** | 10 | 30 | 100 | 7368 | 0.0013 |
| **Caisson** | 10 | 20 | 100 | 1383 | 0.0362 |

Table 1: Pile-soil properties of the 4 considered cases, with $t$ the wall thickness of the pile and $E_s$ the average Young's modulus of the soil profiles.

Note that for the Short-stiff case, and to a lesser extend also the Caisson case, the piles are embedded in very stiff soil; the Young's modulus is in actual fact comparable to that of (weak) rock like shale and sandstone [29]. Although maybe counter-intuitive, the Short-stiff pile is considered a flexible pile by definition of the flexibility factor. For the soil profiles used in this paper, 2 actual seismic cone penetration tests (SCPT) are used that have been previously published [17, 28], called "SCPT20" and "SCPT45". The in-situ density, Young's modulus and estimated Poisson's ratio of both these profiles are given in Figure 5. SCPT45 is the profile of the In-situ case, and SCPT20 is used for the other 3 cases using a scaling factor which is applied to the entire Young's modulus profile: $\frac{1}{12}$, 40 and 10 for the Short-soft, Short-stiff and Caisson case, respectively. These 4 different profiles are used for modelling the 3D SSI and extracting the global stiffness matrices. The SCPT20 profile was also used for the example stiffness matrices given in Figure 3, where it can be seen that the form of the diagonals of these matrices, quite well reflect the shape of the Young's modulus

profile.

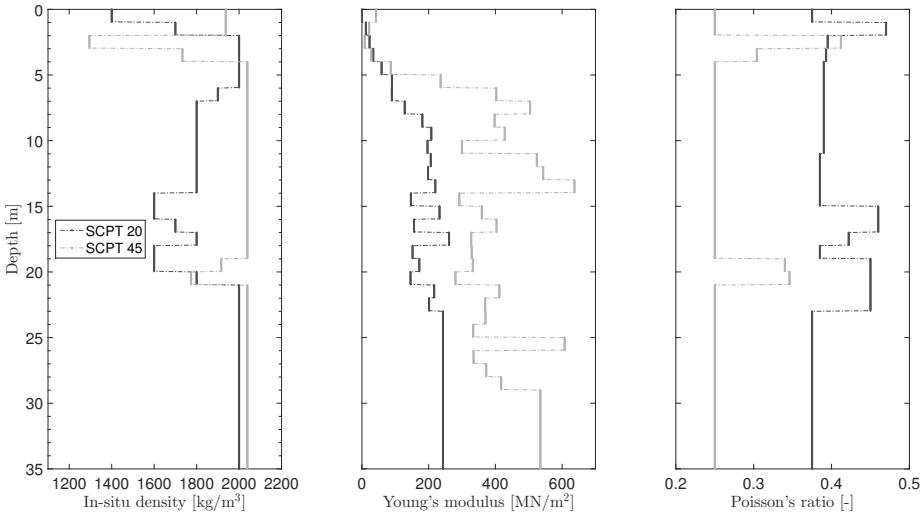


Figure 5: In-situ density, Young's modulus and estimated Poisson's ratio for SCPT20 and SCPT45. SCPT45 is used for the 3D model of the In-situ case, and scaled versions of the Young's modulus of SCPT20 are used for the other 3 cases.

## 3.2. Static response

The 3D SSI solutions in this paper are calculated with a FE model, which employs axisymmetry to decompose the 3D problem into a set of 2D problems; both the soil and the pile are modeled with solid finite elements [30]. As previously mentioned, the pile is assumed to be fully filled with soil. The same model - however, excluding the pile - is used for extracting the global stiffness matrices.

In the next comparisons, the quality of the fit is based on the deflection $u$,

the slope $u' = \frac{du}{dz}$, the rotation $\psi$ and curvature $\psi'$ of the 1D non-local solution compared to those of the 3D model for all depths. The misfit function is defined as

$$
\begin{aligned}
C_{u,u',\psi,\psi'} \quad &= \frac{1}{4}(C_u + C_{u'} + C_\psi + C_{\psi'}) = \\
&\frac{\sum_{i=1}^{i=n} \left|u_{i,1\mathrm{D}} - u_{i,3\mathrm{D}}\right|}{4\sum_{i=1}^{i=n} \left|u_{i,3\mathrm{D}}\right|} + \frac{\sum_{i=1}^{i=n} \left|u'_{i,1\mathrm{D}} - u'_{i,3\mathrm{D}}\right|}{4\sum_{i=1}^{i=n} \left|u'_{i,3\mathrm{D}}\right|} + \\
&\frac{\sum_{i=1}^{i=n} \left|\psi_{i,1\mathrm{D}} - \psi_{i,3\mathrm{D}}\right|}{4\sum_{i=1}^{i=n} \left|\psi_{i,3\mathrm{D}}\right|} + \frac{\sum_{i=1}^{i=n} \left|\psi'_{i,1\mathrm{D}} - \psi'_{i,3\mathrm{D}}\right|}{4\sum_{i=1}^{i=n} \left|\psi'_{i,3\mathrm{D}}\right|},
\end{aligned}
\tag{30}
$$

in which $C_u$, $C_{u'}$, $C_\psi$ and $C_{\psi'}$ are the individual misfits for the corresponding quantities. The comparison of responses for a static horizontal force of $F = 1$ N and an overturning moment $M = 45$ Nm for the 4 cases is given in Figures 6 - 9, where for each case the same coloring is used as in the categorization of Figure 4.

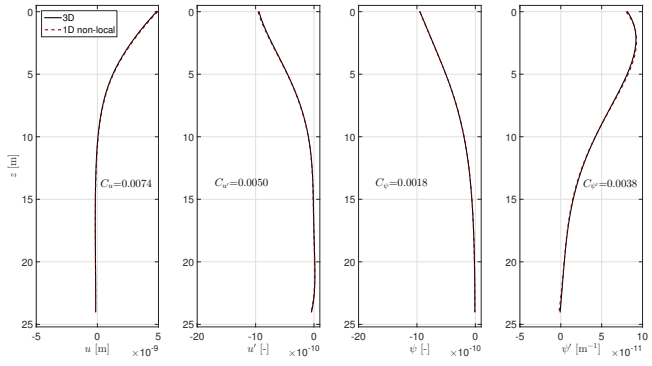


Figure 6: In-situ case, comparison between 1D non-local and 3D solution for a static force of $F = 1$ N and an overturning moment $M = 45$ Nm.

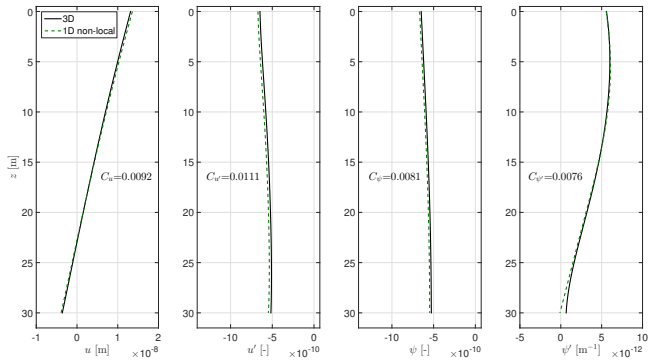


Figure 7: Short-soft case, comparison between 1D non-local and 3D solution for a static force of $F = 1$ N and an overturning moment $M = 45$ Nm.

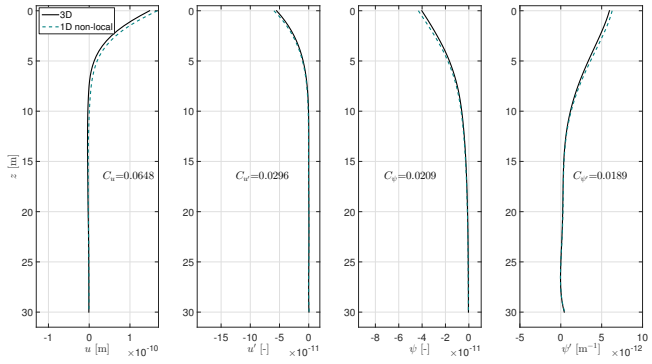


Figure 8: Short-stiff case, comparison between 1D non-local and 3D solution for a static force of $F = 1$ N and an overturning moment $M = 45$ Nm.

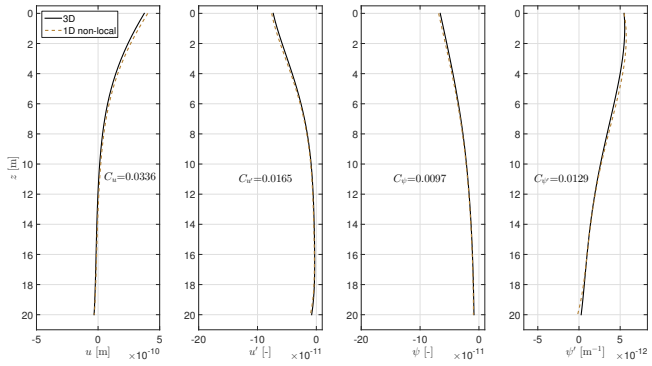


Figure 9: Caisson case, comparison between 1D non-local and 3D solution for a static force of $F = 1$ N and an overturning moment $M = 45$ Nm.

The quality of the fit of the presented cases (Figures 6 - 9) is very good. In the previous work [28], using the local stiffness method for the In-situ case, we reached misfit values of $C_u = 0.0184$, $C_{u'} = 0.0247$, $C_\psi = 0.0096$ and $C_{\psi'} = 0.0197$ ($C_{u,u',\psi,\psi'} = 0.0723$). The misfits associated with the above presented results are summarized in Table 2. Besides the fact that the misfits using the here presented non-local technique are almost twice as low, Figures 6 - 9 show that the method is quite insensitive for the type of SSI, demonstrated by the wide range in flexibility factors and different $L/D$ ratios that were chosen for the 4 cases (Figure 4). We do see a somewhat poorer result for the Short-stiff case. Nevertheless, the quality of the fit is still considered satisfactory. Using the local technique [17] for this case would not yield useful results. Furthermore, we emphasize that the newly developed non-local stiffness technique is a direct approach, whereas the local technique requires optimization, involving much

more uncertainty (and computational cost) than the non-local stiffness method.

| | $C_{u,u',\psi,\psi'}$ | $C_u$ | $C_{u'}$ | $C_\psi$ | $C_{\psi'}$ |
|---|---|---|---|---|---|
| **In-situ** | 0.0179 | 0.0074 | 0.0050 | 0.0018 | 0.0038 |
| **Short-soft** | 0.0360 | 0.0092 | 0.0111 | 0.0081 | 0.0076 |
| **Short-stiff** | 0.1342 | 0.0648 | 0.0296 | 0.0209 | 0.0189 |
| **Caisson** | 0.0727 | 0.0336 | 0.0165 | 0.0097 | 0.0129 |

Table 2: Misfits (Eq. 30) for the 4 SSI cases, static solution (Figures 6 - 9).

## 3.3. Dynamic response

The previously discussed 3D FE model (Section 3.2) incorporates, for the dynamic case (frequency domain[1]), perfectly matched layers, as defined in [31]. These layers are used at the outer boundary of the domain to avoid wave reflections. For very low frequencies, the perfectly matched layers are replaced by elastic layers whose dimensions are large enough so that the artificial boundaries do not influence the results. In order to keep the calculation times small, the size of the elements composing these buffer layers are made successively larger as the distance to the pile increases. To account for energy loss due to the hysteretic behaviour of soil, the shear modulus of the soil $G_s$ is made complex

[1]In this paper, we use the Fourier transform $F(\omega) = \int_{-\infty}^{\infty} f(t)\mathrm{e}^{-\mathrm{i}\omega t}dt$ to transform the equations to the frequency domain.

by including the input soil material damping ratio $\zeta$ [32]:

$$G_s^* = G_s(1 + \mathrm{i}\eta\mathrm{sgn}(\omega)) = G_s(1 + 2\mathrm{i}\zeta\mathrm{sgn}(\omega)), \tag{31}$$

where $\eta$ is the loss factor. The material and the geometric damping cause the soil response and thus the global stiffness matrices (Eqs. 12 - 15) to become complex valued. A 1% ($\zeta = 0.01$) material damping was assigned to all layers in the 3D models. The 1D equilibrium equations (Eqs. 8 and 9) for the dynamic case, written in the frequency domain, become

$$\begin{aligned} GA\kappa\Big(\frac{d^2u(z)}{dz^2} - \frac{d\psi(z)}{dz}\Big) - \int_0^L \mathring{K}^{\mathrm{u,u}}(z,\overline{z})u(\overline{z})d\overline{z} & \\ - \int_0^L \mathring{K}^{\mathrm{u,\Psi}}(z,\overline{z})\psi(\overline{z})d\overline{z} + \omega^2\rho A u(z) &= 0, \end{aligned} \tag{32}$$

$$\begin{aligned} GA\kappa\Big(\frac{du(z)}{dz} - \psi(z)\Big) + EI\frac{d^2\psi(z)}{dz^2} - \int_0^L \mathring{K}^{\mathrm{\Psi,\Psi}}(z,\overline{z})\psi(\overline{z})d\overline{z} & \\ - \int_0^L \mathring{K}^{\mathrm{\Psi,u}}(z,\overline{z})u(\overline{z})d\overline{z} + \omega^2\rho I\psi(z) &= 0, \end{aligned} \tag{33}$$

containing complex-valued stiffness kernels $\mathring{K}^{\mathrm{u,u}}(z,\overline{z})$, .. ,$\mathring{K}^{\mathrm{\Psi,u}}(z,\overline{z})$, lateral inertia $\rho A$ and rotary inertia $\rho I$, with $\rho$ the mass density of the pile. Apart from the steel mass, the pile is assumed to be fully filled with the same soil as outside of the pile. The frequency-dependent inertia forces of the soil are automatically incorporated in the complex-valued stiffness matrices, which are calculated with the obtained frequency response, see Eqs. 12 - 15.

The resulting comparison of the dynamic response of the 3D and 1D mod-

els for the 4 cases, excited by a harmonic horizontal force of $F(\omega) = 1$ N, an overturning moment $M(\omega) = 45$ Nm and excitation frequency $f = 0.3$ Hz ($\omega = 2\pi f = 1.88$ rad/sec) is given in Figures 10 - 13. This excitation frequency is rather arbitrary, nevertheless, a frequency of $f = 0.3$ Hz is surely below the first resonance frequency of these soil-pile systems, ensuring a stiffness-dominated response (rather than inertia-dominated), which is the focus of this paper. Furthermore, $f = 0.3$ Hz is close to the typical first natural frequency of offshore wind turbine structures.

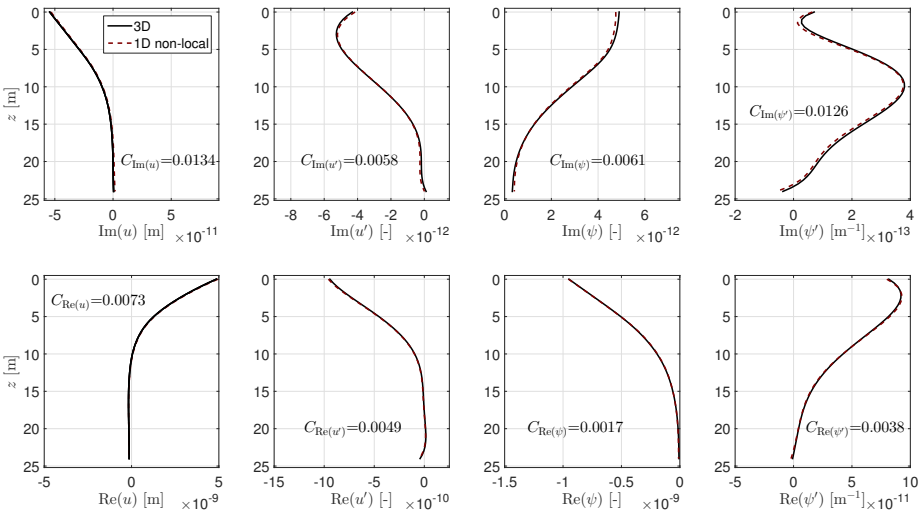


Figure 10: In-situ case, comparison between 1D non-local and 3D solution for a harmonic force of $F = 1$ N and overturning moment $M = 45$ Nm at a frequency of $f = 0.3$ Hz.

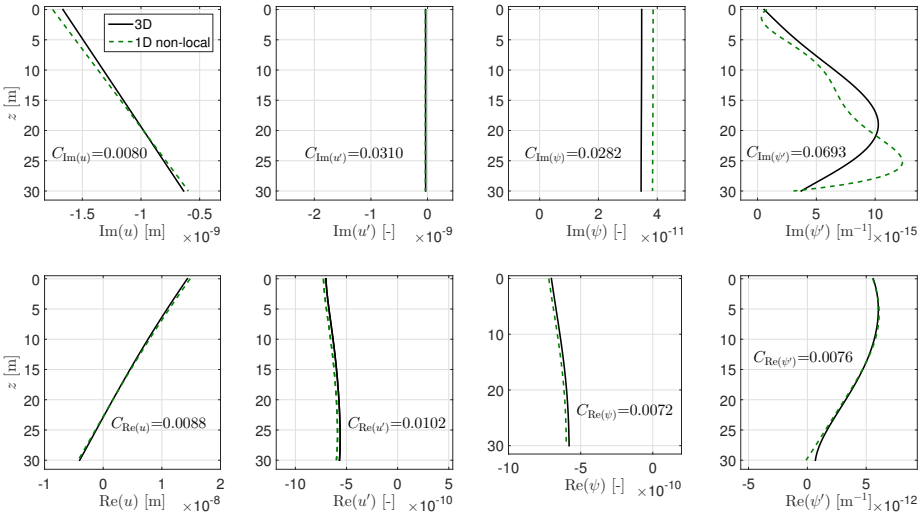


Figure 11: Short-soft case, comparison between 1D non-local and 3D solution for a harmonic force of $F = 1$ N and overturning moment $M = 45$ Nm at a frequency of $f = 0.3$ Hz.

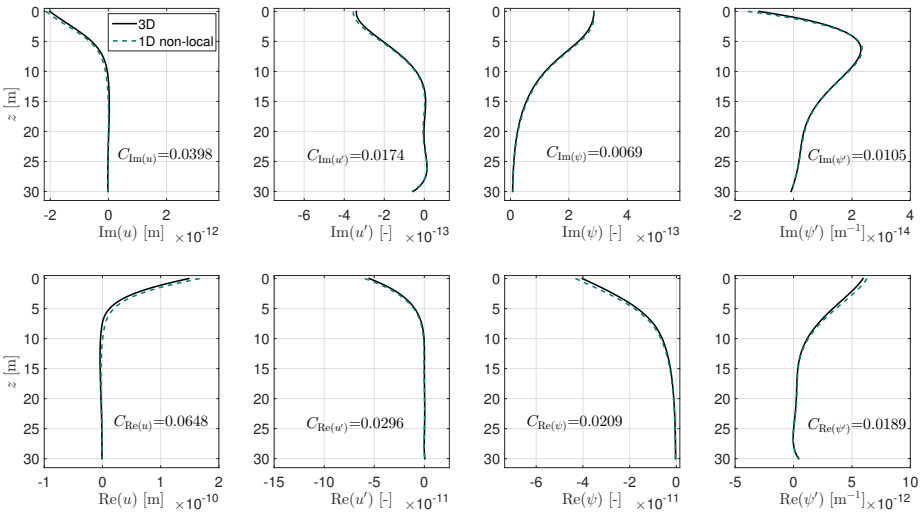


Figure 12: Short-stiff case, comparison between 1D non-local and 3D solution for a harmonic force of $F = 1$ N and overturning moment $M = 45$ Nm at a frequency of $f = 0.3$ Hz.

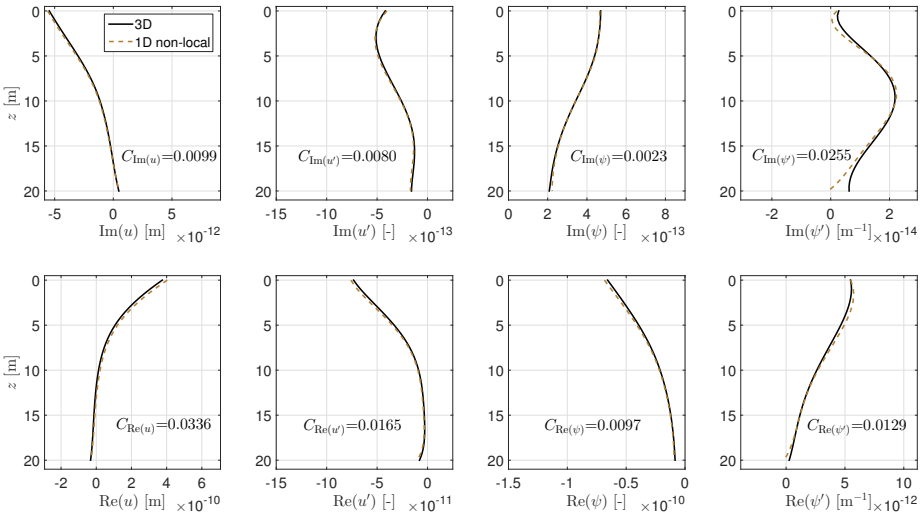


Figure 13: Caisson case, comparison between 1D non-local and 3D solution for a harmonic force of $F = 1$ N and overturning moment $M = 45$ Nm at a frequency of $f = 0.3$ Hz.

The fits for the imaginary and real parts of the response in case of a dynamic excitation, as presented in above Figures 10 - 13, are very satisfactory. The misfits of the imaginary parts ($C_{\mathrm{Im}(..)}$) are comparable to those of the real parts ($C_{\mathrm{Re}(..)}$). In some cases they are larger than the misfit of the real part; for instance, $C_{\mathrm{Im(u)}} > C_{\mathrm{Re(u)}}$ for the In-situ and Short-soft cases (Figures 10 and 11, respectively). However, the opposite also occurs ($C_{\mathrm{Im(u)}} < C_{\mathrm{Re(u)}}$) for the Short-stiff and Caisson cases (Figures 12 and 13, respectively). Although the imaginary part of the rotations of the Short-soft case are matched quite well, the misfit for the derivative $C_{\mathrm{Im}(\psi')}$ is quite high. The misfits of the above presented results are summarized in Table 3.

| | $C_{u,u',\psi,\psi'}$ | | $C_u$ | | $C_{u'}$ | | $C_\psi$ | | $C_{\psi'}$ | |
|---|---|---|---|---|---|---|---|---|---|---|
| | **Re** | **Im** | **Re** | **Im** | **Re** | **Im** | **Re** | **Im** | **Re** | **Im** |
| **In-situ** | 0.0178 | 0.0379 | 0.0073 | 0.0134 | 0.0049 | 0.0058 | 0.0017 | 0.0061 | 0.0038 | 0.0126 |
| **Short-soft** | 0.0338 | 0.1365 | 0.0088 | 0.0080 | 0.0102 | 0.0310 | 0.0072 | 0.0282 | 0.0076 | 0.0693 |
| **Short-stiff** | 0.1342 | 0.0747 | 0.0648 | 0.0398 | 0.0296 | 0.0174 | 0.0209 | 0.0069 | 0.0189 | 0.0105 |
| **Caisson** | 0.0727 | 0.0456 | 0.0336 | 0.0099 | 0.0165 | 0.0080 | 0.0097 | 0.0023 | 0.0129 | 0.0255 |

Table 3: Misfits (Eq. 30) for the 4 SSI cases, dynamic solution (Figures 10 - 13). The misfits are defined for the real (Re) and imaginary (Im) parts of the solutions.

Similar efforts in matching 3D and 1D responses have been performed in [16]. As opposed to these authors, we do not aim to develop general relations between 3D and 1D SSI stiffness parameters; we developed a technique to accurately translate the 3D SSI into 1D effective parameters for each case. In [16], a 20% accuracy of the pile head displacement and a 13% accuracy for the pile head rotations is reached (the responses over the soil depths are not addressed), for a pile of 2 m diameter, length of 8 m, embedded in a 3-layer soil profile with an average $E_s = 25$ MPa, and an excitation frequency of 5 Hz. For the presented cases, we reach an *overall* (for all $z$) accuracy range of 3.43% (Short-soft case) - 24.16% (Short-stiff) for the magnitude (absolute values) of the displacements $u(z)$ and 4.45% (Caisson) - 5.57% (Short-stiff) for the magnitude of the rotations $\psi(z)$. Note that Table 3 gives the misfits of the imaginary and real parts of the response separately, not of the absolute values (which are considered in [16]). In case of only considering the mudline correspondence - as is often done - we reach

a 1.92% (In-situ) - 11.15% (Short-stiff) accuracy for the displacement $u(0)$, and 1.61% (In-situ) - 6.89% (Short-soft) for the rotation $\psi(0)$.

## 4. Discussion

The presented fits of both the static and dynamic responses of the 1D models with those of the 3D models are very satisfactory, and within accuracy limits that are acceptable for structural designers. Nevertheless, although this 1D non-local approach could be considered an exact equivalent modelling method for the 3D models, there are still differences between the responses of these 2 models.

One cause could be the difference between the modelling methods of the pile: the 1D Timoshenko beam versus the solid elements used in the 3D model. To further investigate this difference, 3 other cases were considered. First a static cantilever pile (to exclude the soil reaction) with $L = 25$ m, $D = 5$ m and $t = 60$ mm was analyzed using the 3D FE solid elements, and the 1D FD solution. The overall mismatch in deflections between these two models was $C_u = 0.0068$, which is small, but is of the same order as the values presented for the static SSI cases in Table 2. For completeness we note that the misfit of the FD solution and the analytical solution for a 25 m cantilever beam gave

an error for the deflection of $C_u = 5.997 \cdot 10^{-5}$ for $h = 0.5$ m. In the second comparison, a Timoshenko beam FE model embedded in a 3D solid continuum (with the same pile properties as the cantilever, and a similar soil profile as SCPT20, Figure 5) was compared to the 3D model as used in the previous sections (solid elements to model the pile). The third case is similar to the second, but employs shell elements for the 3D pile. The misfit of deflections for these two cases was $C_u = 0.0020$ for the pile meshed with solid elements and $C_u = 0.0068$ for the pile meshed with shell elements. Again, these values are small, but not negligible and they are of the same order as the values presented in Table 2. Obviously, these misfit values will vary for different pile geometries and soil combinations. The difference in 3D and 1D pile modelling is expected to be the main cause for the higher misfit obtained for the Short-stiff case; the ovalisation of the 3D pile in this high soil-stiffness case was verified to be higher than that in the Short-soft case (having the same pile geometry, but softer soil). We can conclude that the modelling difference between a 3D pile and the used beam theory can be a cause of the remaining mismatch between the observed 3D and 1D responses.

The modelling difference between a 3D pile and the beam theory could fur-

thermore cause an inaccuracy in the modelled interaction of the pile with the soil; to extract the global stiffness matrices, beam-shaped (rigid ring) deformations are prescribed to the soil, whereas the 3D soil-pile model allows for circumferential dependance of the displacements.

Additionally we note that, in case an even higher accuracy is required, the small remaining difference in stiffness can be easily further diminished by optimizing the global stiffness matrices, leading to lower misfits. Multiplying the global stiffness matrices by a factor $\alpha$ - to be optimized - can compensate for the above discussed difference in 3D pile and beam theory.

## 5. Conclusions

In this paper we have demonstrated a novel technique to mimic the complex 3D dynamic response of a vast range of soil-pile systems with a 1D beam on non-local Winkler foundation model. It was shown how to extract the global soil stiffness matrices from the 3D, inhomogeneous continuum, and how to incorporate them in a 1D model, which can subsequently serve as a condensed substructure that can be connected to other design models. Since obtaining the global stiffness matrices is a one-time action, the gain lies in the computational time that can be saved in employing the non-local, reduced-order 1D model in

extensive design simulations. The explained procedure is straightforward and fast, can be easily automated, and does not require any optimization to acquire acceptable results. The global stiffness matrices automatically capture all the 3D mechanisms occurring in the interaction of (large-diameter) piles and soil, removing the need for any empirical tuning factors that relate 3D soil parameters to their 1D effective parameter. Four SSI cases are presented with $L/D$ ratios varying between 2 and 5, and a range of average Young's modulus of the soil between 15 and 7400 MPa. Very satisfactory fits are found between the response of the 3D and 1D models over the full embedded length, in terms of the displacement, slope, rotation and curvature, for both static and dynamic excitation. The presented work provides the engineering design community with dual benefit of accuracy of a 3D model in defining the stiffness, mass and damping properties of an SSI system, and the computational speed of a 1D model.

## 6. Acknowledgement

The work is part of the "DISSTINCT" project - a 4-year research project of Siemens Wind Power, Fugro, Delft University of Technology and DNV-GL aimed at improved dynamic soil characterization and modelling for offshore wind turbines [33], [34]. The DISSTINCT project is partly funded by the Dutch

government (project number TKIW02001), for which the authors would like to express their gratitude.

## References


[1] E. Winkler, Die Lehre von der und Festigkeit, Dominicus, Prague, Czech Republic.

[2] J. V. Boussinesq, Application des potentiels a l'étude de l'équilibre et du mouvement des solides élastiques., Vol. 4, Gauthier-Villars, 1885.

[3] A. Flamant, Sur la répartition des pressions dans un solide rectangulaire chargé transversalement, CR Acad. Sci. Paris 114 (1892) 1465–1468.

[4] P. L. Pasternak, On a new method of analysis of an elastic foundation by means of two foundation constants, Gosudarstvennoe Izdatelstvo Literaturi po Stroitelstvu i Arkhitekture, Moscow.

[5] R. Di Laora, E. Rovithis, Kinematic bending of fixed-head piles in nonhomogeneous soil, Journal of Geotechnical and Geoenvironmental Engineering 141 (4) (2014) 04014126.

[6] P. Cuéllar, Pile foundations for offshore wind turbines: Numerical and experimental investigations on the behaviour under short-term and long-term cyclic loading, Ph.D. thesis, Technical University of Berlin, Faculty VI - Planen Bauen Umwelt (2011). doi:10.14279/depositonce-2760.

[7] S. Corciulo, O. Zanoli, F. Pisanò, Transient response of offshore wind turbines on monopiles in sand: role of cyclic hydro–mechanical soil behaviour, Computers and Geotechnics 83 (2017) 221–238.

[8] K. Terzaghi, Evaluation of coefficients of subgrade reaction, Geotechnique 5 (4) (1955) 297–326.

[9] H. Zimmermann, Die Berechnung des Eisenbahn Oberbaues (The Calculation of Railway Superstructures), Ernst & Korn, Berlin, 1888.

[10] H. Matlock, Correlations for design of laterally loaded piles in soft clay, in: Offshore Technology in Civil Engineering: Hall of Fame Papers from the Early Years, ASCE, 1970, pp. 77–94.

[11] L. C. Reese, W. R. Cox, F. D. Koop, Analysis of laterally loaded piles in sand, Proceedings of the 6th Annual Offshore Technology Conference, Houston, Texas, USA, (OTC 2080) (1974) 473–484.

[12] M. W. O'Neill, J. M. Murchinson, Fan Evaluation of p-y Relationships in Sands, Tech. rep., A report to the American Petroleum Institute (1983).

[13] S. Soerensen, L. Ibsen, A. Augustesen, Effects of diameter on initial stiffness of p-y curves for large-diameter piles in sand, numerical methods in geotechnical engineering, in: Proc. of the 7th European Conference, Trondheim/Norway, Vol. 2, 2010.

[14] D. Kallehave, C. L. Thilsted, M. Liingaard, Modification of the API p-y formulation of initial stiffness of sand, in: Offshore Site Investigation and Geotechnics: Integrated Geotechnologies - Present and Future. Proceedings of the 7th International Conference on Offshore Site Investigations and Geotechnics, London, Society of Underwater Technology, 2012, pp. 465–472.

[15] L. Andersen, J. Clausen, Impedance of surface footings on layered ground, Computers & Structures 86 (1) (2008) 72–87.

[16] Varun, D. Assimaki, G. Gazetas, A simplified model for lateral response of large diameter caisson foundations - linear elastic formulation, Soil Dyn. Earthq. Eng. 29 (2) (2009) 268–291.

[17] W. G. Versteijlen, A. V. Metrikine, K. N. van Dalen, A method for identification of an effective winkler foundation for large-diameter offshore wind turbine support structures based on in-situ measured small-strain soil response and 3D modelling, Engineering Structures 124 (2016) 221–236.

[18] Y. Lei, M. I. Friswell, S. Adhikari, A galerkin method for distributed systems with non-local damping, International Journal of Solids and Structures 43 (11) (2006) 3381 – 3400. doi:http://dx.doi.org/10.1016/j.ijsolstr.2005.06.058.

[19] M. I. Friswell, S. Adhikari, Y. Lei, Non-local finite element analysis of damped beams, International Journal of Solids and Structures 44 (22) (2007) 7564 – 7576. doi:http://dx.doi.org/10.1016/j.ijsolstr.2007.04.023.

[20] M. Damgaard, L. V. Andersen, L. B. Ibsen, Dynamic response sensitivity of an offshore wind turbine for varying subsoil conditions, Ocean Engineering 101 (2015) 227–234.

[21] K. F. Graff, Wave Motion in Elastic Solids, Oxford University Press, 1975.

[22] A. T. de Hoop, Handbook of Radiation and Scattering of Waves: Acoustic Waves in Fluids, Elastic Waves in Solids, Electromagnetic Waves, Academic Press, 1995.

[23] J. van Kan, A. Segal, F. Vermolen, Numerical Methods in Scientific Computing, VSSD, 2005.

[24] K. T. Brødbæk, M. Møller, S. P. H. Sørensen, A. H. Augustesen, Review of p-y relationships in cohesionless soil, Tech. Rep. 57, Aalborg University (2009).

[25] H. G. Poulos, T. S. Hull, The role of analytical geomechanics in foundation

engineering, in: Foundation engineering: Current principles and practices, ASCE, 1989, pp. 1578–1606.

[26] C. N. Abadie, Cyclic Lateral Loading of Monopile Foundations in Cohesionless Soils, Ph.D. thesis, University of Oxford (2015).

[27] J. E. Bowles, Foundation Analysis and Design, McGraw-Hill, New York, 1996.

[28] W. G. Versteijlen, F. W. Renting, P. L. C. van der Valk, J. Bongers, K. N. van Dalen, A. V. Metrikine, Effective soil-stiffness validation: Shaker excitation of an in-situ monopile foundation, Soil Dyn Earthq Eng 102 (2017) 241–262.

[29] R. Weijermars, Principles of Rock Mechanics, Alboran Science Publishing, 1997.

[30] O. C. Zienkiewicz, R. L. Taylor, The Finite Element Method for Solid and Structural Mechanics, Butterworth-heinemann, 2005.

[31] E. Kausel, J. M. Oliveira Barbosa, PMLs: A direct approach, International Journal for Numerical Methods in Engineering 90 (3) (2012) 343–352.

[32] J. D. Achenbach, Wave Propagation in Elastic Solids, Vol. 16, North-Holland Publishing Company - Amsterdam, 1973.

[33] W. G. Versteijlen, S. N. Voormeeren, Efficient support structure design through improved dynamic soil structure interaction modeling, Tech. rep., TKI-WoZ Project Description, DISSTINCT (2013).

[34] TKI Wind op Zee DSSI project (DISSTINCT), `http://tki-windopzee.nl/project/dssi`, accessed: 2016-08-10.